Large-Eddy Simulation of a Rocket Nozzle Undergoing End Effects

F. Burdairon*o[†], G. Daviller*, C. E. Tinney°, S. Blanchard°
°CNES, Space Transportation Directorate - 52, Rue Jacques Hillairet, 75612 Paris Cedex - FRANCE
°Applied Research Laboratories, The University of Texas at Austin, Austin, USA, 78758
*CERFACS - 42 av. G. Coriolis 31057 Toulouse Cedex 01 - FRANCE
burdairon@cerfacs.fr · simon.blanchard@cnes.fr · daviller@cerfacs.fr · charles.tinney@arlut.utexas.edu
†Corresponding author

Abstract

A Large Eddy Simulation (LES) of the flow through a thrust optimized parabolic contour nozzle (TOP) is developed for nozzle pressure ratios corresponding to the End Effects Regime (EER). EER is known to generate significant nozzle side-loads and vibroacoustics loads during startup and is of practical importance to many high-lift launch vehicles. The TOP nozzle is characterized by a design Mach number of $M_d = 5.24$ and an exit-to-throat area ratio of $A_j/A^* = 30.29$. LES predictions of the static wall pressure along the nozzle wall are shown to compare favorably to laboratory-scale measurements of the same TOP contour, while the predicted peak frequency associated with the fore and aft motion of the separation shock is also complementary to unsteady pressure measurements acquired near the nozzle lip. A qualitative comparison of the exhaust flow and shock pattern at discrete instances in time in the LES are also shown to comprise many of the features captured using a high speed schlieren system; both databases reveal large radial displacements of the supersonic annulus during EER due to intermittent venting of the last annular separation bubble with the ambient air. Spatially resolved snapshots of the wall shear stress from the LES reveal the typical tee-pee like shock patterns which are commonly observed in full-scale rocket engine testing. The LES framework is shown to provide all of the pertinent physics needed to understand the mechanism responsible for generated EER side loads.

1 Introduction

The startup and shutdown of large area ratio nozzles used for heavy lift rocket launch vehicles can generate significant off-axis loads depending on the nozzle contour. These side loads are detrimental to the safety of both crew and payload¹ and have been responsible for premature failure of mission critical hardware². The sources of these side loads are driven by the different flow and shock patterns the form on the inside of the nozzle, which depend on the nozzle geometry and Nozzle Pressure Ratio³ (NPR; the ratio of plenum pressure P_0 to ambient pressure P_a). During startup, the flow first experiences Free-Shock Separated (FSS) flow at low NPRs in which the supersonic flow detaches from the wall to form a separated flow region made up of a series of compression and expansion waves^{4,5}. This forms a low-pressure subsonic recirculating region immediately following the separation shock and along the nozzle wall that communicates directly with the ambient air. If the nozzle contour is a thrust-optimized parabolic (TOP), as is often the case (in order to maximize performance at high altitude), the flow may transition to a Restricted Shock Separated (RSS) flow where the detached region of supersonic flow reattaches downstream of the separation line to form a series of separation bubbles at the nozzle wall⁶. FSS→RSS transition generates the first large nozzle side load⁷ and occurs at a nozzle pressure ratio during startup that is different from the one corresponding to RSS—FSS transition during shutdown^{2,8}. The source of this hysteresis is caused by differences in the position of the intersection between the internal shock and the separation shock relative to the triple point and is well known⁹. Depending on the length of the TOP nozzle wall, multiple separation and reattachment points can form during RSS flow, as shown by Nguyen et al. (2003)¹, thereby leading to a series of trapped annular separation bubbles whose locations depend on NPR. At higher NPRs, and well above FSS → RSS transition, a second critical NPR range exists in which the last annular separation bubble approaches the nozzle lip and begins to open intermittently to the ambient air. The intermittent breathing is characterized by large fore and aft motions of the separation shock along the nozzle wall and is the next significant source of nozzle side loads⁷, which often exceeds the loads generated during FSS \rightarrow RSS transition; this is the so-called End-Effects Regime (EER) described by Nave and Coffey (1973)¹⁰.

Over the years there has been a considerable amount of attention focused on characterizing the sources of nozzle side loads using laboratory-scale hardware and standard instruments like schlieren, static and dynamic wall pressure transducers and particle image velocimetry^{11,12,6,8}. However these instruments fall short of accurately capturing details about the flow inside the nozzle, which is needed if one is to close the scientific gap concerning the mechanisms responsible for EER nozzle side loads. In this regard, high-fidelity numerical models capable of simulating the three-dimensional internal flow and shock pattern states offer valuable insight into regions where experiments are less effective, and is needed if this outstanding problem of scientific importance is to be solved. Numerical models of the uniquely different flow states that form during startup of high area ratio nozzles are often developed using a Reynolds Average Navier-Stokes (RANS) framework, and by imposing restrictive assumptions in order to generate low-cost solutions in a timely manner. Allamaprabhu et al. (2016)¹³ evaluated several common RANS turbulence closure models (Spalart-Allmaras, $k-\varepsilon$, $k-\omega$ and the shear stress transport (SST) model) of separated flows in various overexpanded nozzle contours and reported a sensitivity in the separation shock location to the type of closure model used in the numerical scheme. More recently, Afkhami et al. $(2023)^{14}$ showed that the SST and the Generalized k- ω (GEKO) models overpredicted both the turbulence kinetic energy and the separation shock location. The latter of these two models was able to recover the separation shock location after some corrections, albeit the RANS framework is incapable of capturing shock transients, which are fundamental to the nozzle side load problem. The unsteady-RANS (URANS) approach offers some relief to the numerical community. For example, Lijo et al. (2010)¹⁵ developed a URANS solution of an overexpanded TOP nozzle during both startup and shutdown using the Reynold stress turbulence model, and managed to reproduce the FSS ↔ RSS hysteresis. Martelli et al. (2010)⁹ also modeled the same hysteresis by generating simulations of the FSS and the RSS regimes at the same NPR. Their model captured the unsteady motion of the Mach disk in the RSS flow state, but was limited to piston-like motions due to symmetry assumptions invoked in the model.

The development of higher fidelity numerical models that can accurately capture the three-dimensional characteristics of the flow and shock patterns in these high area-ratio nozzles, and in particular, the azimuthal asymmetries responsible for generating nozzle side loads, is a prerequisite to solving this problem. One such development is that of the Detached-Eddy Simulation (DES) and Delayed DES (DDES) approaches where the unsteady regions are resolved using a Large-Eddy Simulation (LES) framework, while the attached flow is modeled with RANS 16,17,18,19,20. One such example can be found in the work of Deck 2009¹⁷, who developed a three-dimensional DDES of the flow through a thrust-optimized parabolic (TOP) contour nozzle while undergoing EER. In this study, the nonstationary RSS flow was investigated while large oscillations associated with EER were captured. Favorable comparisons of the wall pressure profile and azimuthal asymmetries have also been reported with these approaches¹⁸. However, because of the costly and ambitious undertaking of the DES/DDES/LES frameworks, only a few studies concerning shock dynamics have been reported in the open literature. Some examples include that of Olson and Lele (2011)²¹ who reported unsteady motions of the Mach disk in a planar nozzle during FSS state and showed good comparison to experiments. Conversely, to reduce the computational cost, Daviller et al. (2020)²² developed a LES with a static adaptive mesh refinement methodology to accurately capture the FSS flow in a thrust ideal contour (TIC) nozzle²³. While the DES/DDES/LES frameworks offer a promising pathway to modeling these shock and turbulence rich flows, they continue to rely on experimental validation to ensure the appropriateness of the mesh and subgrid scale model needed for numerical dissipation and stability.

The University of Texas at Austin with NASA Marshall Space Flight Center has a rich history in conducting laboratory-scale measurements of the flow and shock pattern states that form in high area ratio nozzles⁵ with particular attention to the vibroacoustic loads generated during EER^{24,8,25}. Some examples include the work of Baars and Tinney (2013)²⁶ who evaluated both steady and transient pressure ratios (startup) of a TOP nozzle and reported the unsteady shock dynamics and its spectral characteristics during RSS flow. Canchero et *al.* (2016)^{8,25} later evaluated clusters of two, three and four TOP nozzles and its immediate sound field using an acoustic imaging technique. The EER flow was shown to generated elevated sound levels relative to other traditional sources of supersonic jet noise (broadband shock associated noise and transonic resonance) while the EER signature resided over a narrow band of frequencies. Shadowgraphy images of the exhaust flow near the nozzle exit during EER revealed an unsteady broadening of the flow immediately outside of the nozzle followed by pulsating motions that generated large coherent structures in the downstream flow. Rojo et *al.* (2016)²⁴ studied the effect of stagger on the startup of clustered nozzles undergoing EER and showed that the overall sound pressure levels (OASPL) at the base of the vehicle can be reduced by as mush as 3 dB with staggered nozzles. Albeit skewness and kurtosis levels remained unaffected thus suggesting that the impulsiveness of the waveforms, which are detrimental to the safety of the vehicle, are still significant when nozzle pressure ratios are staggered between adjacent hardware.

The present work is a preliminary study of the end-effects regime of a high area ratio TOP nozzle that is generated by way of Large-Eddy Simulation. Details concerning the nozzle and test hardware are first described followed by a discussion of the LES framework and a comparison of the model prediction to the experimental measurements. Preliminary results of the model at different points in the flow are reported and discussed using a combination of single

point statistics and dynamic mode decomposition. The findings are used to demonstrate the rich flow and shock physics as captured by the LES model.

2 Experimental and Numerical Configurations

The TOP nozzle used for this study is the one designed by Ruf et al. $(2009)^2$ and has been shown to generate both FSS and RSS flow states, followed by an EER event at relatively low nozzle pressure ratios. The nozzle shape is shown in Fig. 1a alongside a computer aided design rendering in Fig. 1b. The nozzle contour has a throat diameter of $D^* = 12.7$ mm, a length of $x_L = 79.375$ mm (measured from the throat curvature to the nozzle lip), and an exit diameter of $D_e = 69.9$ mm resulting in an area ratio of $A_e/A^* = 30.3$. This corresponds to a design Mach number of 5.24 and would be achieved with a pressure ratio of 700. This particular nozzle has been studied extensively over the years by Canchero et al. $(2016)^{25}$ and Rojo et al. $(2016)^{24}$, and is a truncated version of the nozzle reported by Baars et al. $(2012)^5$, and Martelli et al. $(2020)^{20}$. The principal focus of this study will be the operating condition associated with the EER.

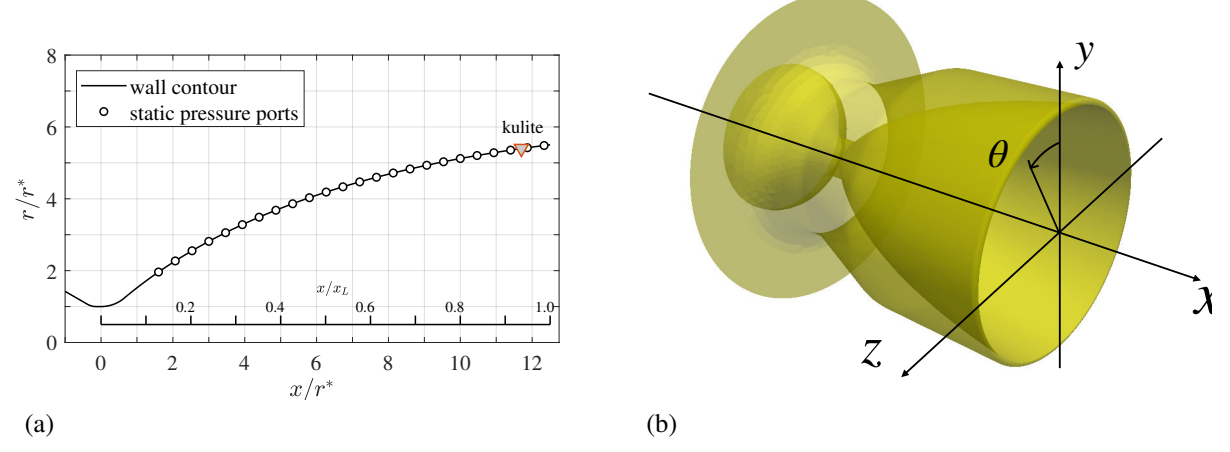


Figure 1: (a) Thrust optimized parabolic nozzle contour with location of static pressure sensing ports. (b) CAD rendering of the TOP nozzle with coordinate system.

2.1 Experimental setup

The laboratory-scale measurements reported here were performed in the Gas Dynamics Laboratory (GDL) of the Applied Research Laboratories, The University of Texas at Austin (ARL:UT). The GDL is an acoustically treated facility enclosing 850 m³ of air space over 140 m² of floor space and houses several high pressure test stands. The working fluid is unheated air and is provided by way of a four-stage compressor that removes oil and water using a condensate separator during high stages of compression. Nozzle hardware is mounted to a test stand elevated 2.5 m above the floor and centered on a large opening in the GDL facility wall. Outside air is allowed to enter the GDL through several large openings in the back of the facility; these openings provide sufficient entrainment for the expanding jet plumes while preventing the building from collapsing. The gas delivery system is a blow-down type with pressurized air (up to 145 bar) being stored in several tanks encompassing 6.2 m³ of water volume storage. Nozzle pressure ratio is the key determinant of the different operating states of the TOP nozzle hardware and is monitored and recorded using various pressure and temperature sensors located in the nozzle plenum and throughout the GDL.

Static and dynamic wall pressure sensors, as well as a z-type schlieren system, were used to generate an assortment of databases for model validation. Starting with the static wall pressure p_s , various ports located along the length of the nozzle wall are connected to several Scanivalve DSA3218 Digital Pressure Scanner with each module comprising 16 temperature compensated piezoresistive pressure sensors with $\pm 0.05\%$ full-scale accuracy that are digitized using 16 bit A/D converters at a 440 Hz sample rate. The locations of these ports are provided in Fig. 1a while an image of the TOP nozzle during testing is provided in Fig. 2a.

Unsteady wall pressure signatures that form during nozzle start up are captured using a single Kulite model XT-140-2100A transducer placed near the nozzle lip at $x/r^* = 11.7$. The location of the sensor is chosen specifically to capture the unsteady motion of the last trapped annular separation bubble during EER. The Kulite was recorded at a 20 kHz sample rate and was installed with the protective B-screen flush with the interior surface of the nozzle wall. As

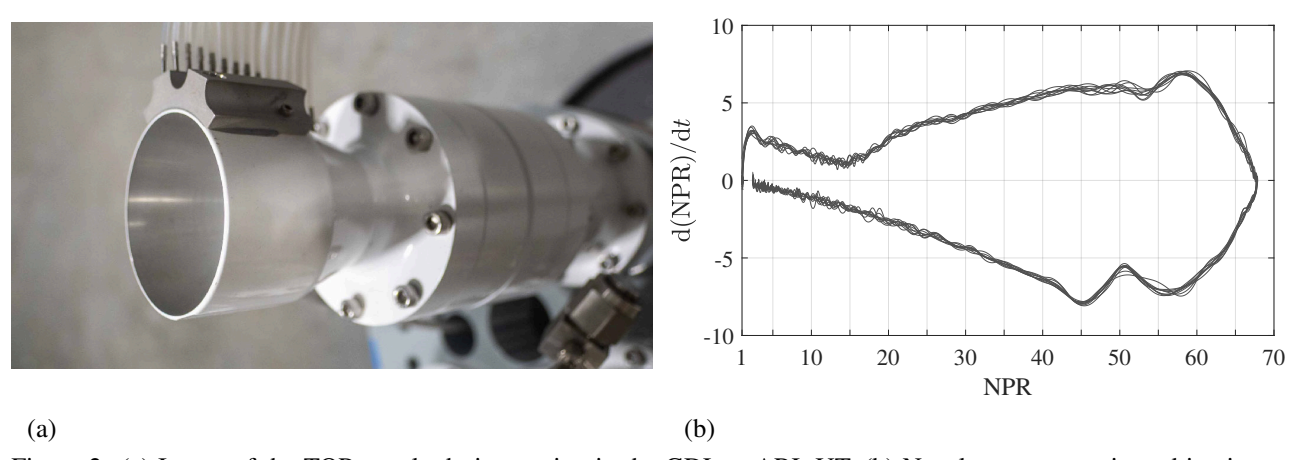


Figure 2: (a) Image of the TOP nozzle during testing in the GDL at ARL:UT. (b) Nozzle pressure ratio and its time derivative for ten consecutive tests.

for the schlieren system, this comprised a z-type setup with a 510-540 nm (green) light-emitting-diode light source, an i-SPEED 726 monochromatic camera manufactured by iX Cameras, and two 31.75 cm diameter gold-coated parabolic mirrors with 2.54 m focal length. A dedicated pair of linear translation stages provided accurate positioning of the mirrors while the optics with razor blade were aligned to accommodate a 90 deg cutoff. The i-SPEED 726 camera has 2048×1536 pixels that are $13.5~\mu m$ in length with 12-bit depth. For this study, schlieren images were captured uninterrupted at a 100~kHz frame rate.

Static and dynamic wall pressures were recorded during several slow transient startups and shutdowns of the TOP nozzle using the ramp rate curves shown in Fig. 2b. On the other hand, schlieren measurements were acquired during both steady and transient operations with an emphasis on conditions leading up to, and including, EER. The repeatability of the sample ramp rates shown in Fig. 2b demonstrates the consistency of the test apparatus.

A contour diagram of the static wall pressure during startup of this TOP nozzle is shown in Fig. 3a alongside slices of the wall pressure at discrete nozzle pressure ratios in Fig. 3b. A dashed line identifies the location of the separation shock which shifts abruptly downstream around NPR= 22 when the shock structure undergoes FSS→RSS

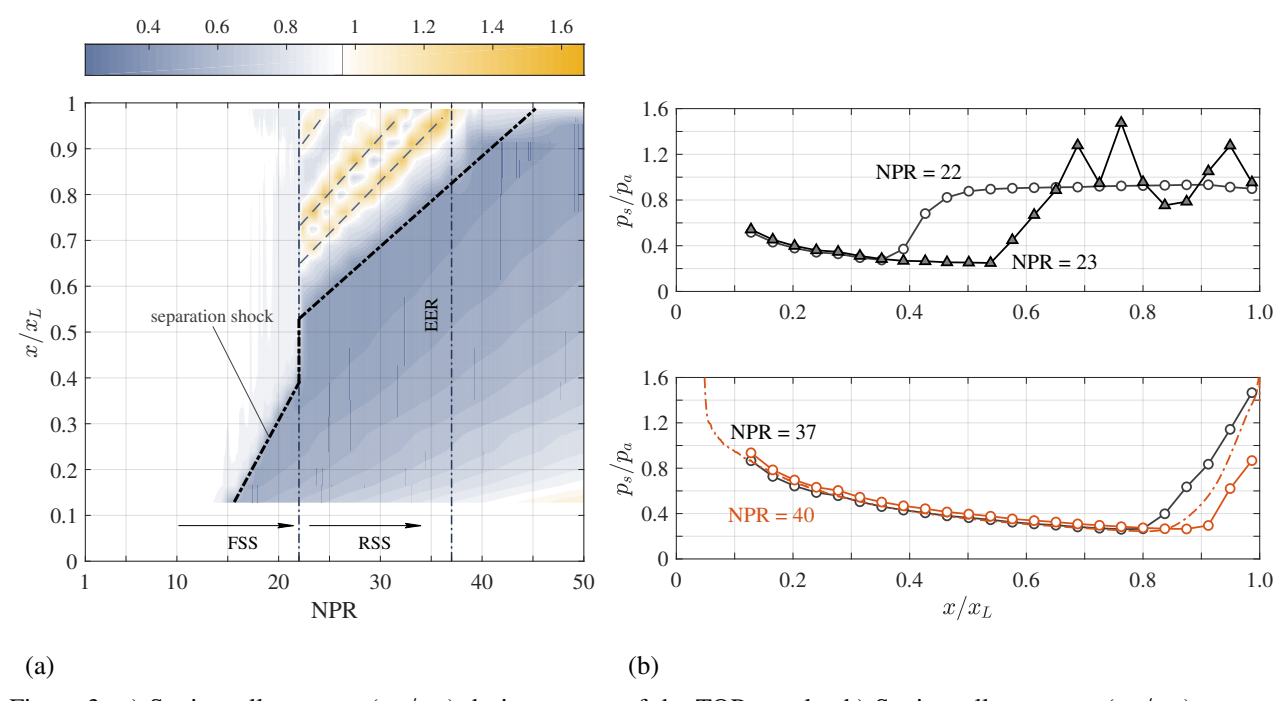


Figure 3: a) Static wall pressure (p_s/p_a) during startup of the TOP nozzle. b) Static wall pressures (p_s/p_a) corresponding to FSS, RSS and EER flow states. The dash-dotted line corresponds to the LES data and the circle symbols to the experiment.

transition. The RSS structure is also identified by the formation of several high-pressure subsonic annular separation bubbles which is more clearly seen in Fig. 3b. As NPR increases, the RSS structure pushes out of the nozzle with the last trapped annular separation bubble residing near the nozzle lip around NPR= 37; this is when the onset of EER occurs. It should be pointed out that FSS→RSS transition, as well as EER, may vary slightly with NPR for the same nozzle contour. That is, schlieren images acquired during FSS→RSS transition (not shown) have revealed opposing sides of the nozzle undergoing transition at different times with one side appearing to be in the RSS state, while the other is still in FSS. This partial FSS→RSS transition has been observed elsewhere and is responsible for the first high side load event during startup. As for EER, this occurs between NPR= 37 and 38.5 for this nozzle. The variations in nozzle pressure ratio corresponding to both FSS→RSS transition and the EER event are exacerbated in full-scale systems on account of asymmetries in the nozzle shape, changes to surface roughness and stiffness along the nozzle wall, material stresses and deformations from previous firings, and varying gas species due to incomplete combustion.

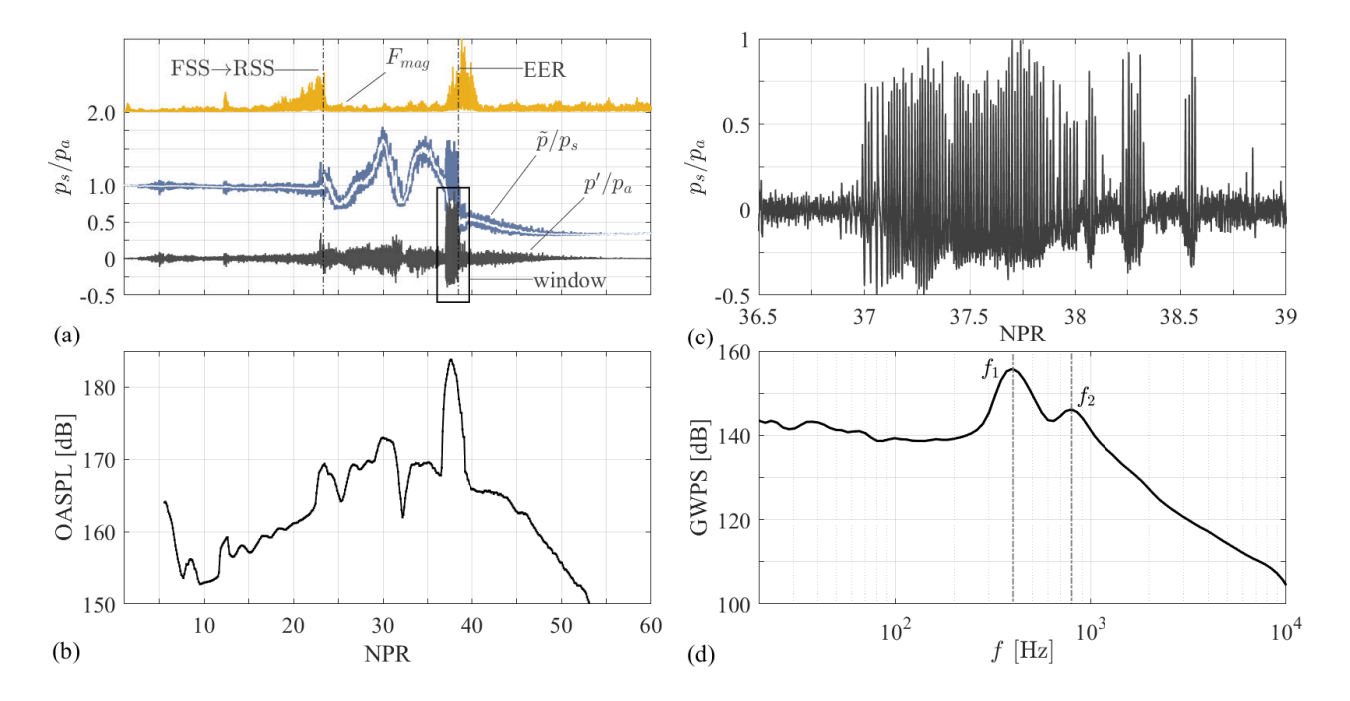


Figure 4: (a) Kulite pressure time-series during startup aligned with measure of nozzle side loads (F_{mag}). (b) Moving window averaged OASPL [dB] of kulite pressure time series. (c) Close up of kulite pressure reading identified by the window in (a) during EER. (d) Global wavelet power spectrum between $37 \le \text{NPR} \le 38$.

The dynamic wall pressure captured using the kulite sensor near the nozzle lip is shown in Fig. 4a where it is separated into its mean and fluctuating components ($\tilde{p} = P + p'$) using the decimate command in Matlab and an 8th order Chebyshev Type I lowpass filter. Pressure data are aligned with arbitrarily-scaled nozzle side load magnitudes (F_{mag}) ; these side loads are measured using the strain tube method described by Tinney et al. $(2025)^{27}$ and the references therein. The findings reinforce the notion that the largest amplitude side loads occur during both FSS

RSS transition and EER. A moving average window is then used to calculate the pressure variance shown in Fig. 4b and expressed in dB (re: 20μ Pa). The peak dynamic pressure during EER is registered at 183.7 dB and occurs at NPR= 37.65. Closer inspection of the fluctuating pressure in Fig. 4a during EER is shown in Fig. 4c where the onset of the fore and aft shock motion occurs at NPR= 37 and continues mostly uninterrupted until NPR= 38, after which a few intermittent events appear, which fade by NPR= 38.6. A time-frequency analysis of the fluctuating pressure timeseries using Morlet wavelets is computed using the process described by Baars and Tinney (2013)²⁶. From the wavelet power spectrum, the Global Wavelet Power Spectrum (GWPS, re: 20μ Pa) is computed by averaging the WPS between $37 \le NPR \le 38$. The findings are shown in Fig. 4d and reveal two distinct peaks at $f_1 = 396$ Hz and $f_2 = 793$ Hz. The first peak coincides with the fore and aft motions of the separation shock along the nozzle wall and the cyclic venting of the trapped annular separation bubble with the ambient air. The second, higher frequency peak is a harmonic of the first peak frequency and is attributed to a double pulsing motion of the shock as it moves in and out of the nozzle.

A random sequence of schlieren images at NPR 37 are shown in Fig. 5. The images demonstrate the different flow patterns that form during EER resulting from the fore and aft motion of the separation shock. In Fig. 5a, the supersonic annulus on the upper and lower surfaces of the nozzle appear identical, thus suggesting that the location of

the separation shock is the same for the upper and lower nozzle surfaces. The next image in Fig. 5b reveals a large vortical structure being ejected from the nozzle and rolling up approximately one nozzle diameter downstream. The supersonic annuli have steeper angles, thus demonstrating how the separation shock is closer to the nozzle lip than in Fig. 5a. Moving to Fig. 5c, the upper and lower supersonic annuli have different shapes while the plume is biased towards the upper part of the image. This asymmetry is the consequence of differences in the separation shock locations on the upper and lower surface, which is responsible for generating the nozzle side loads during EER. Another large roll-up structure is beginning to form downstream of the nozzle lip in Fig. 5d while the supersonic annuli are the same for the upper and lower surfaces. The sequence of images support the notion that then the location of the separation shock is the same on the upper and lower surfaces of the nozzle, that its fore and aft motions generate large vortical structures coinciding with the column structure appearing in conventional jet flows. On the contrary, large asymmetries in the separation shock location, which are responsible for generating nozzle side loads, generate flapping motions in the downstream shear layer.

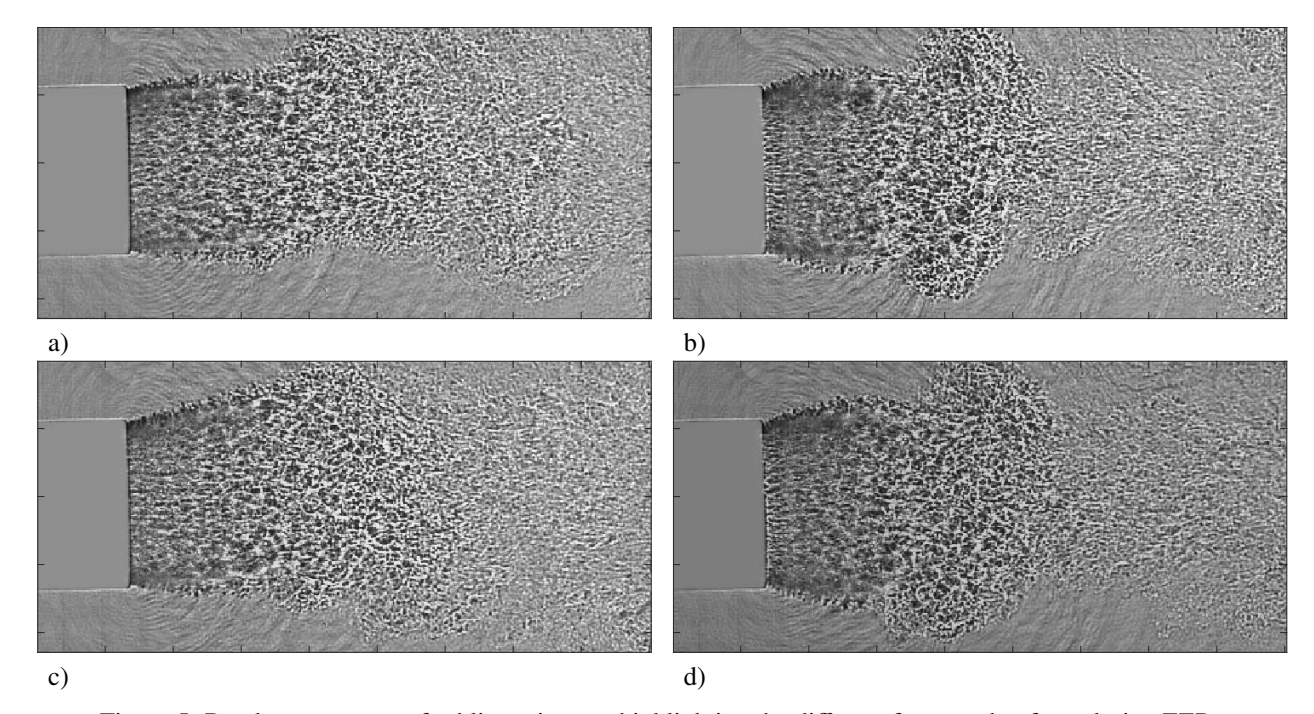


Figure 5: Random sequence of schlieren images highlighting the different features that form during EER.

2.2 Numerical setup

The unsteady simulation presented in this study is based on the LES methodology developed at CERFACS^{28,29} and is carried out using an explicit, unstructured, and highly parallel AVBP solver³⁰. The compressible Navier-Stokes equations are solved using the second-order Lax-Wendroff finite volume scheme in both space and time³¹. Viscous fluxes are computed using the 2Δ diffusion operator³², while an artificial viscosity operator of second and fourth order is employed via a local sensor to eliminate spurious numerical oscillations³³. The shock features are treated with a Localized Artificial Diffusivity (LAD) model^{34,35} and a Cook and Cabot hyperviscosity³⁶. Finally, the LES closure is ensured with a subgrid scale SIGMA model³⁷.

The full numerical domain is shown in Fig. 6. Two inlets were used, one to impose the total pressure in the convergent nozzle and one to impose a small co-flow that helps to evacuate the jet flow to the outlet. The latter is located far away from the nozzle, and takes the shape of a semi-hemispheric plenum of radius $r_{out} \sim 63x_L$. The Navier-Stokes Characteristic Boundary Conditions (NSCBC) are applied to both inlets and the outlet³⁸. An isothermal coupled wall model³⁹ at temperature $T_w = 293$ K is applied on the internal walls of the nozzle, and an adiabatic noslip condition on the external walls. The wall unit discretization is about $y^+ \sim 50$ near the separation shock location, which is shown in Fig. 3b to occur around $x/x_L = 0.8$ for this NPR. The mesh is composed of 150×10^6 tetrahedral elements. Moreover, a small step is introduced at the transition between the convergent and the throat to help trigger the turbulence in the internal boundary layer, following the methodology proposed by Langenais et $al.^{40}$ as shown at the bottom right in Fig. 6. The flow is initialized as in Daviller et $al.^{22}$, using Eq. (1), where P_a is valued at 101325 Pa for the LES.

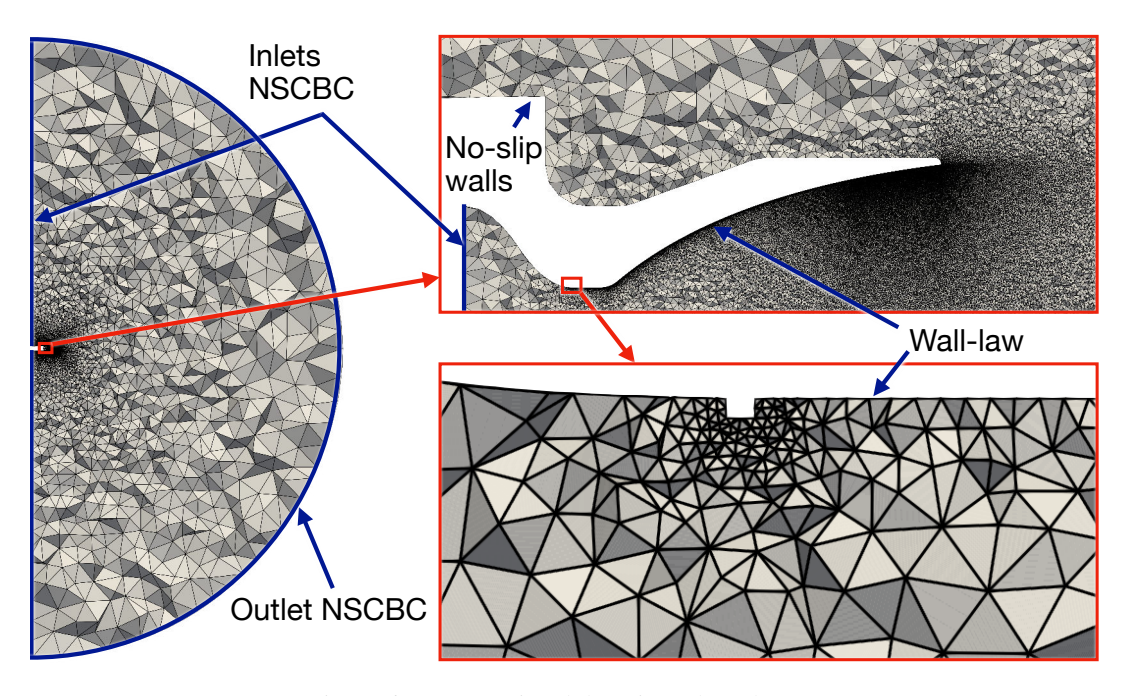


Figure 6: Computational domain and mesh

$$P = P_a + f_{tan}(P_0 - P_a) \tag{1}$$

$$f_{tan} = 1 - \frac{1}{2} \left(1 + \tanh\left(\frac{x - 0.6x_L}{0.4x_L}\right) \right)$$
 (2)

The computation is done on an in-house cluster equipped with AMD bisocket Genoa 9654 CPUS at 2.4 GHz. The flow is first initialized on a coarse mesh of approximately 6 million tetrahedral cells over 100 ms using 360 cores for 18h. The solution is then interpolated onto a fine mesh, and after another transient time of 3 ms, the statistics are gathered over 35 ms, corresponding to approximately twelve EER periods according to the experimental measurements reported in Fig. 4d and confrimed later through a spectral analysis of the LES solution. A total of 180 CPU hours using 1920 cores are used to complete the simulation. As for post-processing, on-the-fly interpolations in the XY and XZ planes are recorded at a sampling frequency of 50 kHz. Data are then stored within a smaller volume encompassing both a region inside the divergent section of the nozzle and a portion downstream of the nozzle exit, and at a reduced sampling frequency of 20 kHz. Numerical probes are also inserted at various points within the flow and are recorded at a much higher sampling frequency of approximately 1.3 MHz. Signal processing is then conducted using the Antares library⁴¹.

3 LES of an over-expanded jet flow in End-Effect Regime

Due to the intrinsically intermittent and unstable nature of the EER event, capturing this phenomenon presents a number of challenges numerically. It is also for this reason that this kind of nozzle and flow offer a good benchmark for refining numerical schemes. Prior laboratory measurements have shown that the onset of the End-Effect Regime for this TOP nozzle contour begins around NPR= 37 and can persist as high as NPR= 40. As such, it was decided to generate the LES model at NPR= 40.

To gain an appreciation for the complexity of the overexpanded flow generated by this nozzle, an instantaneous visualization of the velocity magnitude is shown in Fig. 7. The illustration displays the shock patterns inside the nozzle, including the internal shock emanating from the throat, the central lens shock (Mach disk) located within the nozzle near its exit plane, and the lambda shock (RSS) pattern in the RSS flow near the lip. The latter is formed by a separation of the boundary layer, followed by a reattachment located close to the lip. This forms an annular recirculation bubble that is visible on the top wall of the illustration. A large subsonic recirculation region just downstream of the central lens shock is also visible, and is identified at this instant at the bottom of the figure.

A collection of illustrations of Mach number contours from a two-dimensional slice through the XY-plane is shown in Fig. 8 covering one full period of the separation shock motion during the EER event. These snapshots

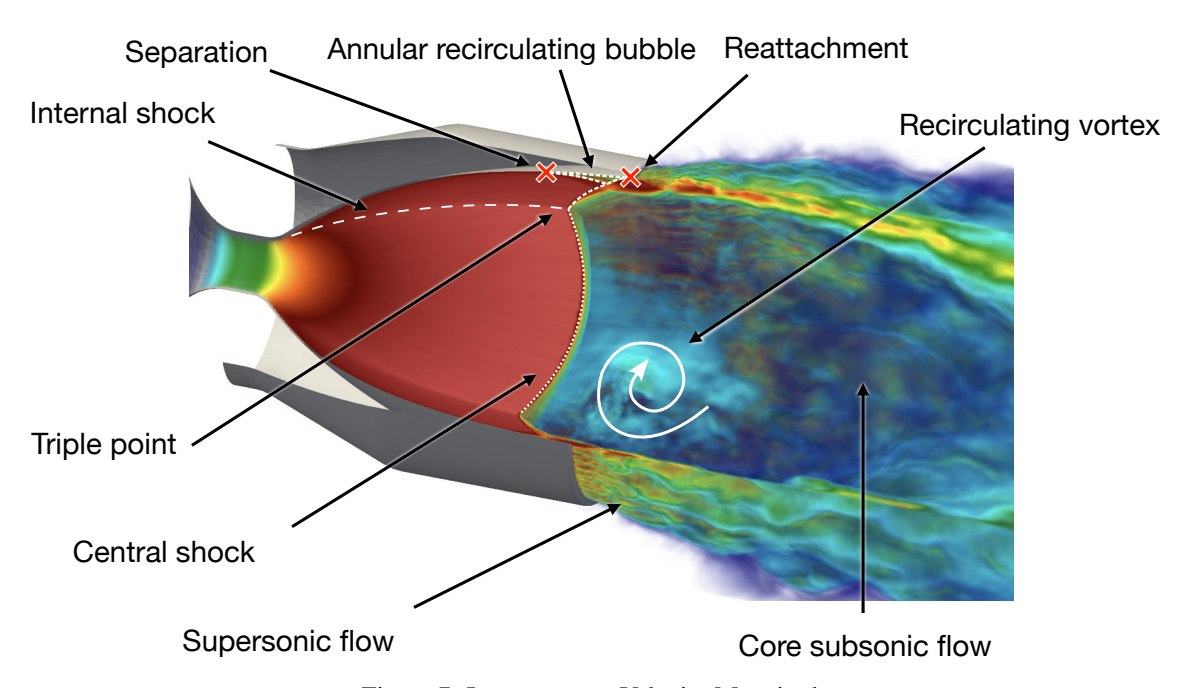


Figure 7: Instantaneous Velocity Magnitude

represent four instants uniformly distributed over one EER period (T=1.4 ms). A vertical white dotted line located at $x/x_L=0.87$ has also been inserted in each illustration in order to highlight the motion of the central lens shock during this EER event period. The same features captured experimentally using the high-speed schlieren in Fig. 5 are complimentary to what is shown here from the LES. In particular, the asymmetry resulting from the separation shock location is visible in this LES. Starting with the first snapshot at $t_1=38.1$ ms in Fig. 8a, the central shock is at its furthest upstream location while the shear layers exiting the nozzle are deflected downward. At $t_2=38.6$ ms, the shock has started to move downstream, the recirculation region reaches the lip, and the supersonic annulus has realigned with the axial direction. By $t_3=39$ ms, the shock is close to the nozzle exit, the separated flow has shifted to a partial-FSS flow, and the supersonic annulus has started to vector radially in a similar fashion to Figs. 5b and 5d. At $t_4=39.54$ ms, the shock pattern has receded upstream, and a di-symmetric vortex structure is visible downstream of the nozzle, similar to what is observed in Fig. 5b.

Having now illustrated the principal features that make up this flow and shock pattern, we will turn towards snapshots of the shear stress distribution along the surface of the nozzle wall to highlight the azimuthal variations in the RSS flow. This is shown in Fig. 9, for the same t_1 and t_3 instances in time corresponding to Figs. 8a and 8c, respectively, while the white dotted line in both illustrations identifies the location of the central lens shock ($x/x_L = 0.87$) at t_1 in Fig. 8a. Contour levels have also been adjusted to highlight the recirculating region along the wall. One can see abrupt changes in the contour level upstream of the dotted line, thus identifying locations along the nozzle wall where the separation shock resides and the flow decelerates abruptly from an expanding supersonic gas with high wall shear stress, to a low wall shear stress subsonic flow immediately downstream of the separation shock 39 . The high wavenumber tee-pee like features are visually identical to images from Baars and Tinney (2013) 26 of large-scale liquid propellant engines during startup thus providing further evidence that the pertinant physics are being captured by this LES model. These pictures also illustrate the motion of the recirculation bubble of the RSS flow while signifying that the length and location are not uniformly distributed in azimuth. Indeed, at t_1 (Fig. 9a) the reattachment line is inside the nozzle, whereas at t_3 (Fig. 9b) it has passed beyond the nozzle lip so that the recirculation bubble is now venting with the ambient air at most locations. Albeit, there are some points, where the separated region is still confined inside the nozzle (around 45° as an example).

In Fig. 3b, the static wall pressure (averaged in azimuth) from the LES at NPR= 40 is compared to the experiments at NPR= 37 and NPR= 40. Prior to shock separation, the mean static wall pressure predicted by the LES aligns well with the experimental results. However, the location of the separation shock predicted by the LES is nestled somewhere between the measurements at NPR= 37 and 40. The discrepancy is attributed to both the effects of azimuthal averaging, which tends to mask the asymmetry of the shock separation, as well as a shorter acquisition time for the LES compared to the experiment.

The pressure signal at the center of the nozzle exit (marked by the red cross in Fig. 8) is shown in Fig. 10. This location is just downstream of the central shock, and corresponds to a lower pressure just below the ambient pressure

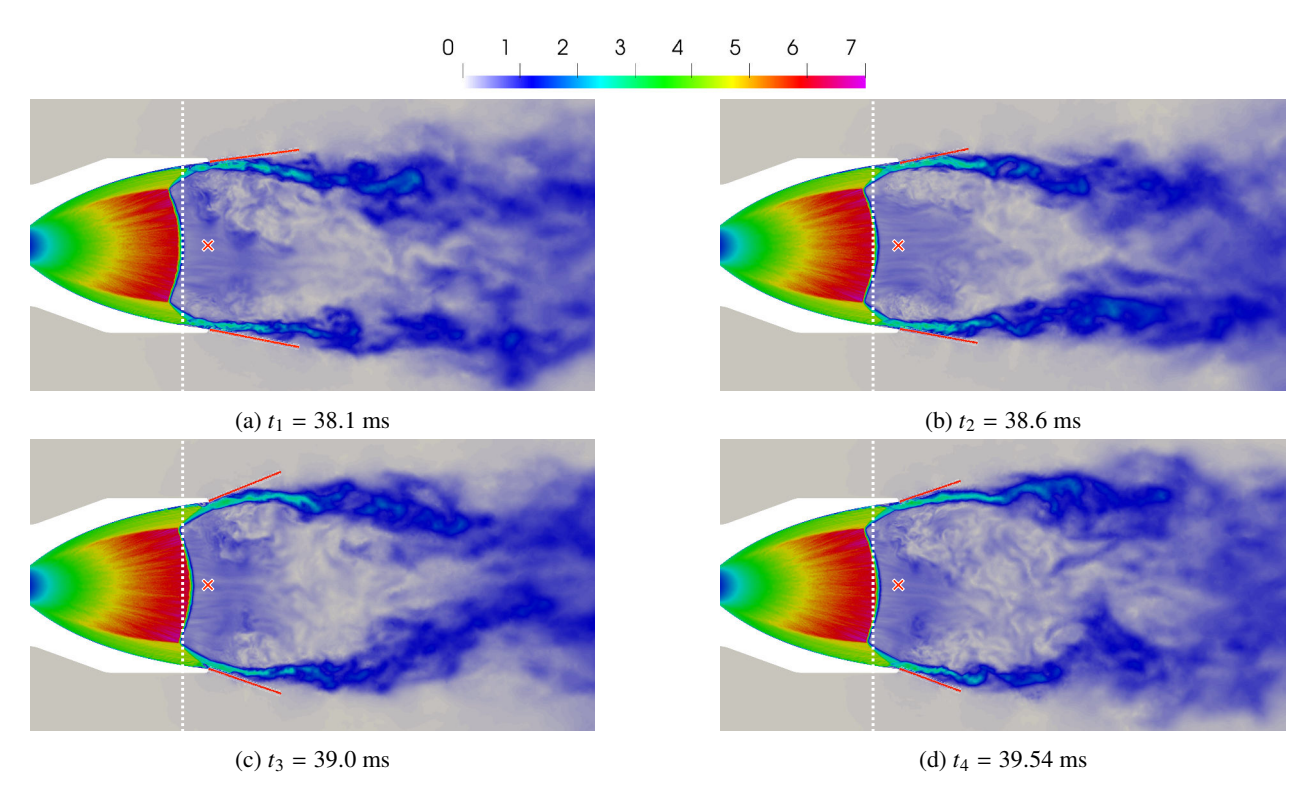


Figure 8: Instantaneous Mach number in the XY-plane at four instances in time covering 1.4 ms. The white dotted line represents the position of the central shock at t_1 , at $x/x_L = 0.87$. The red cross × indicates the location of a probe at the center of the nozzle exit. The red lines follow the external shape of the supersonic jet exiting the nozzle, and open up as the recirculating bubble reaches the lip.

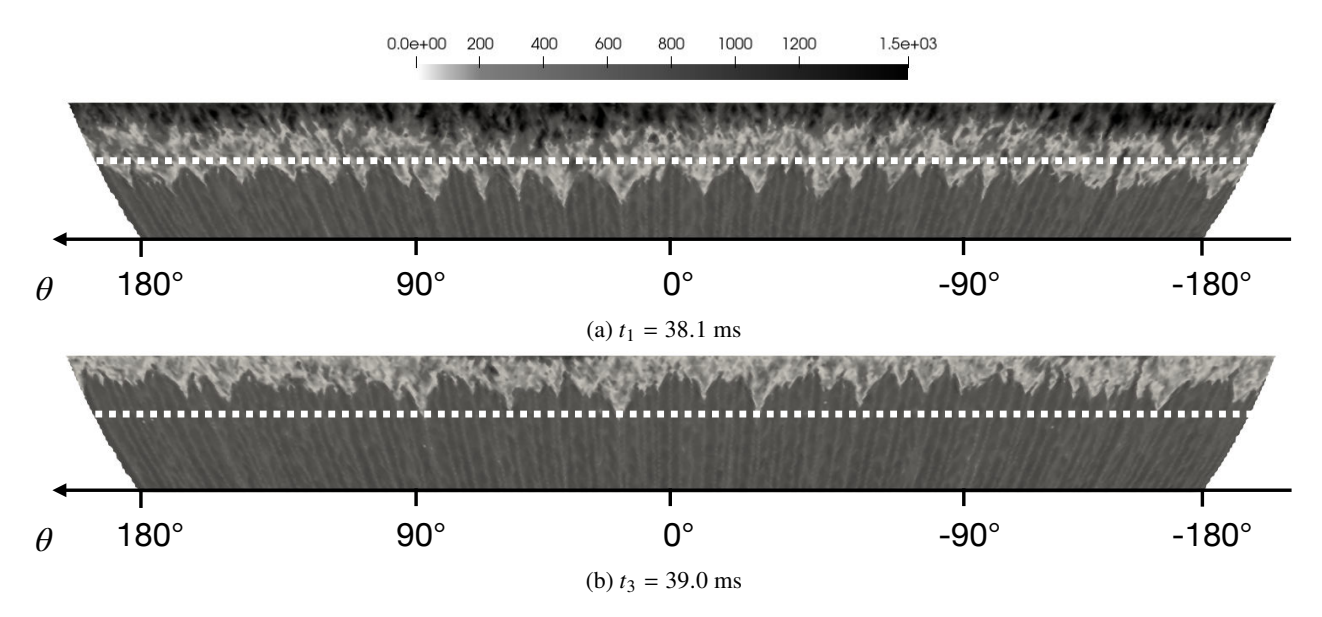


Figure 9: Instantaneous wall shear stress inside the nozzle at (a) $t_1 = 38.1$ ms and (b) $t_1 = 39.0$ ms. The dotted white line is located at $x/x_L = 0.87$.

 P_a . Fig. 10 then illustrates the global displacement of the flow due to the central lens-shaped shock motion. Fig. 10a is the time-evolution over 35 ms, and the vertical lines identify the same four instances in time: $t = t_1, t_2, t_3$ and t_4 . The intermittency of the phenomenon is plainly visible, with a period that evolves between 2 and 3 ms. The Power Spectral Density (PSD) reported in Fig. 10b has been computed by dividing the time-signal into two blocks, followed by a 40% overlap with a Hanning window. The resulted data exhibit a main peak at f = 417 Hz, which is the signature

of the fore and aft motion of the central shock-lens. Moreover, two other peaks at f = 574 Hz and f = 695 Hz are also visible, none of them being a harmonic of the first peak.

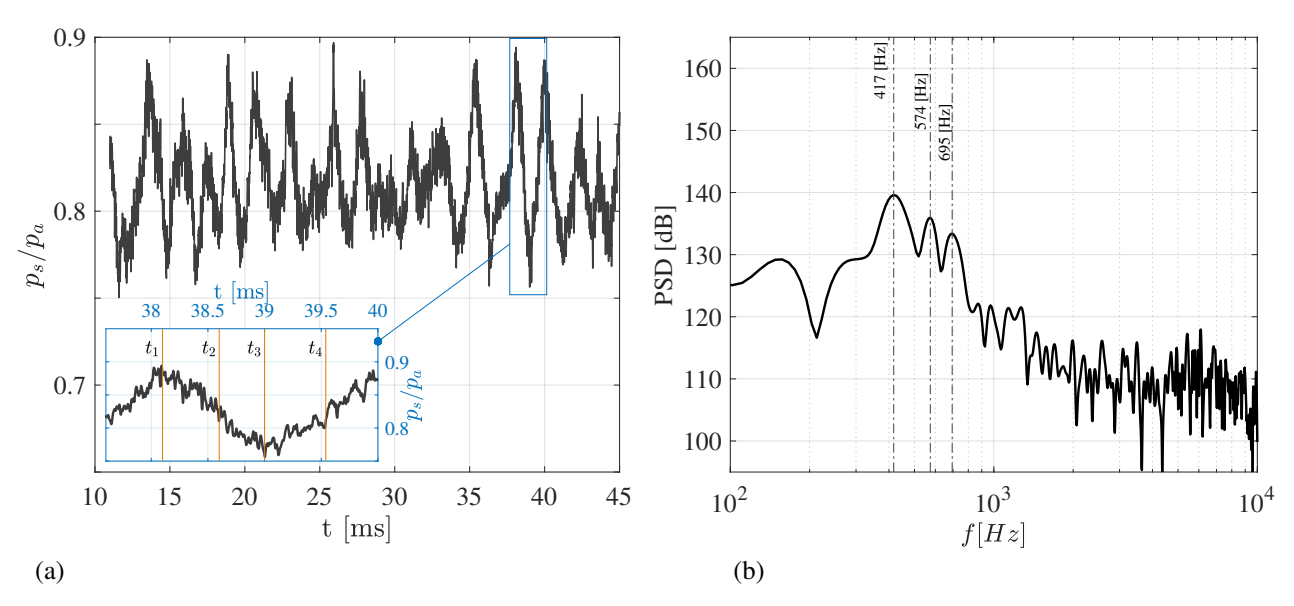


Figure 10: LES prediction of unsteady pressure at the center of the nozzle exit plane. (a) Time-evolution, and (b) PSD, (re: 20μ Pa [dB]). Vertical lines labeled t_1 through t_4 in the figure inset coincide with the instantaneous visualizations in Figure 8

To characterize the asymmetry of the separation shock, the static pressure signal (and corresponding PSD) of four probes around the nozzle lip at the wall (in the nozzle exit plane), at $\theta = 0^{\circ}$, 90° , 180° and 270° are represented in Fig. 11. From the Fig. 11a, it can be observed that the static wall pressure distribution around the lip is not statistically invariant in azimuth for this duration in time, with a preferential direction around the z-axis at $\theta = 90^{\circ}$ and 270° . This is not uncommon and is observed in the moment loci phase diagrams reported by Baars et *al.* .⁵. For the PSD in Fig. 11b, which characterizes the motions of the separation shock, three peaks at f = 417,574 and 695 Hz are identified, similar to te ones observed previously at the center of the nozzle exit. From the experiment, it seems that the signature of the separation shock at $f_1 = 396$ Hz (Fig. 4d) corresponds to those captured in the LES at f = 417 Hz. However, the second peak at $f_2 = 793$ is not recovered in the simulation. It is postulated that this difference may result from the simulation being performed for a fixed NPR = 40, whereas the experiments are conducted with a slow startup sequence, and the mode at f_2 is identified over a range $37 \le NPR \le 38$.

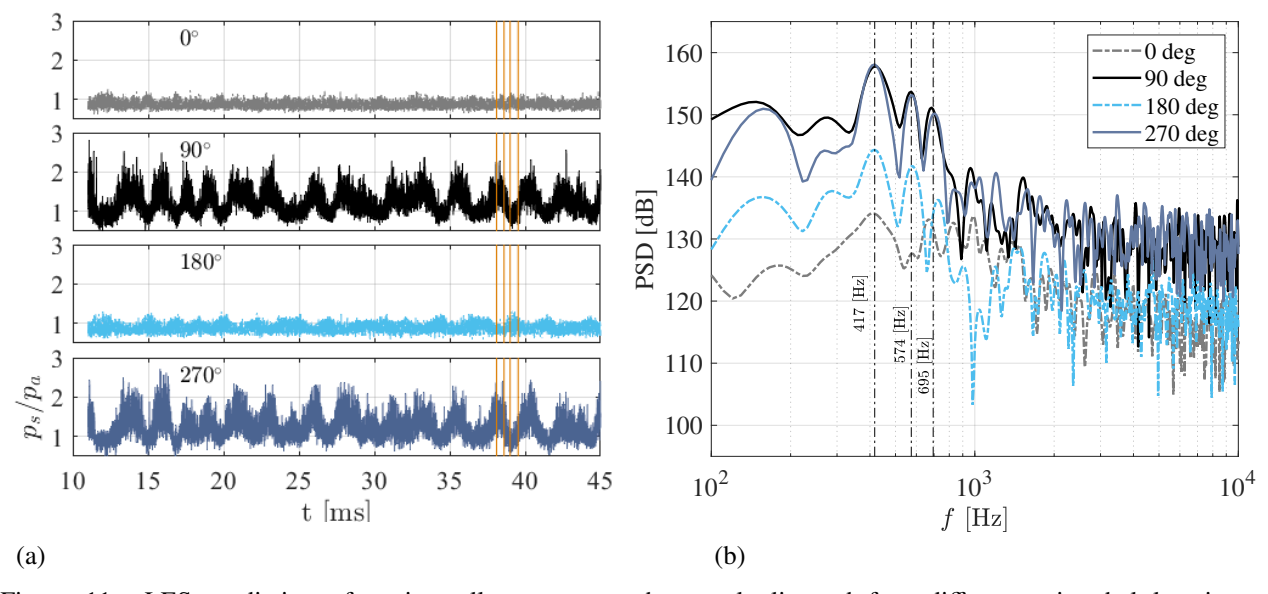


Figure 11: LES prediction of static wall pressure at the nozzle lip and four different azimuthal locations, $\theta = 0^{\circ}$, 90° , 180° , 270° . (a) Time-evolution, and (b) PSD, (re: 20μ Pa [dB]).

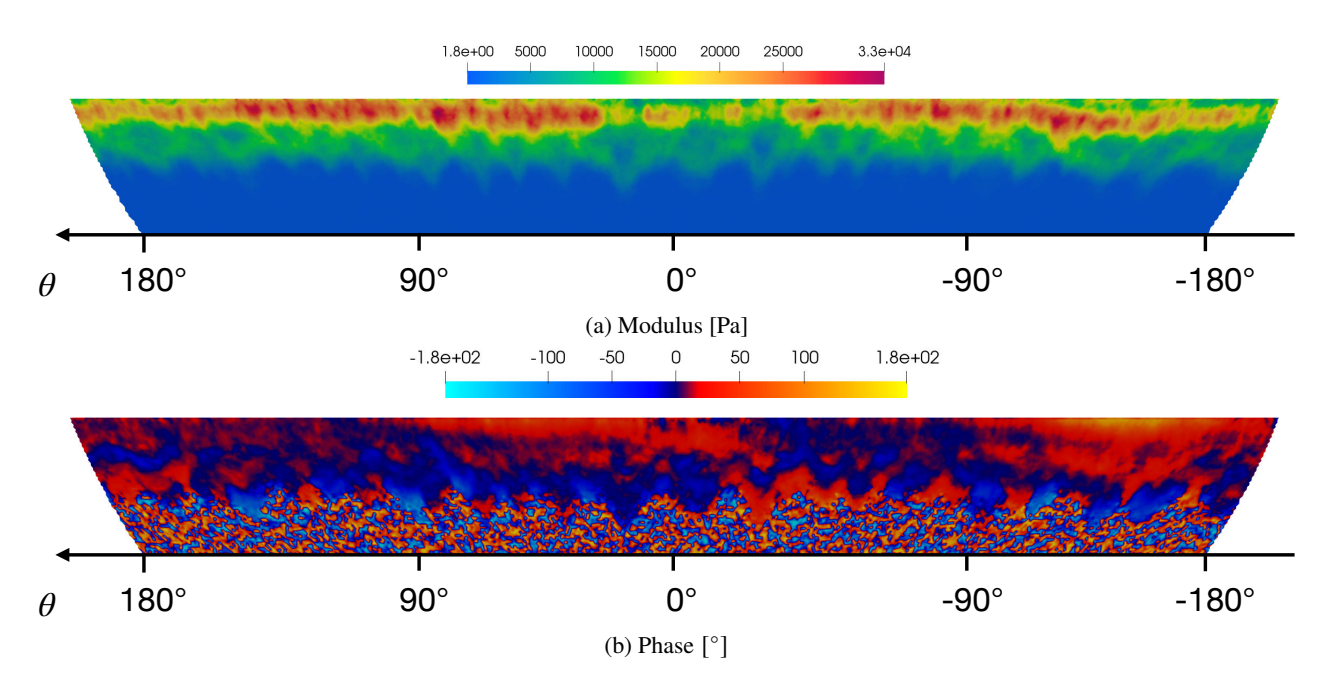


Figure 12: Most energetic mode of the DFT computed on the pressure distribution at the wall (405 Hz)

The signature of the separation shock motion at f = 417 Hz is extracted using a Discrete Fourier Transform on the wall pressure distribution in Fig. 12. The modulus and the phase distributions both display a very asymmetrical pattern around the lip. Most of the energy of this mode is located close to the lip, and around $\theta = 90^{\circ}$ and 270° , which is in agreement with what has been discussed above. According to the phase distribution, these two locations also seem characterized by a phase shift.

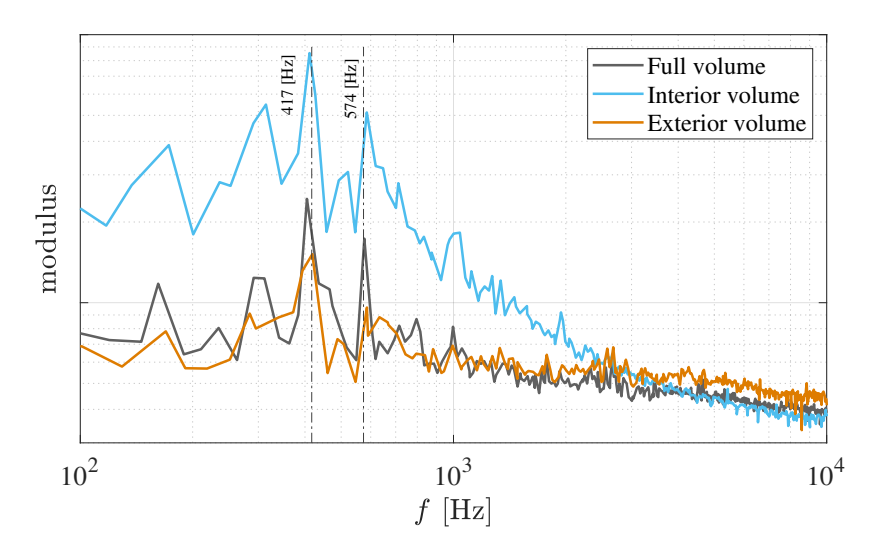


Figure 13: Modulus of modes computed from a DMD of the pressure field inside a volume of flow encompassing a region downstream of the nozzle exit.

Finally, the Dynamical Mode Decomposition 42,34 (DMD) modulus spectrum, performed on the whole interpolation volume, is displayed in Figure 13. Two modes are distinct at f = 407 Hz and f = 577 Hz, in agreement with the local time-signals discussed above. The small discrepancies are attributed to the spectral resolution used to generate the power spectral densities in Figs. 11 and 10. To have a finer insight, DMDs have also been computed on smaller restricted regions, on one hand the inside of the nozzle, and on the other hand the external part outside of the nozzle after the nozzle exit plane. The resulting moduli are very similar and display the same two main modes. This observation suggests that both modes are linked to the central shock and the recirculating bubble at the wall, forming a complex interacting pattern.

4 Summary and conclusion

The first set of results from a Large-Eddy Simulation of the flow through a high area ratio TOP nozzle undergoing End-Effects have been presented. The LES model is compared to laboratory-scale measurements of a smooth wall nozzle with identically shaped contour and the same operating conditions (unheated air). The main features of the nozzle are presented, including the different flow regimes that form during startup. In particular is the FSS flow at low NPR, a FSS→RSS transition at NPR=22, and the onset of the EER event beginning at NPR=37. Characteristics of the static and dynamic wall pressure during EER are displayed with the latter revealing two modes around 396 Hz and 793 Hz. Details concerning the spatially and temporally resolved three-dimensional numerical simulation of the nozzle flow are then presented. The LES model is shown to capture the characteristic intermittency of the EER flow and is accomplished with the assistance of a tripping method that triggers the boundary layer turbulence inside the divergent section of the nozzle. Spatially resolved Mach number contours are shown at discrete instances in time and reveal the displacement of the central shock, the venting of the recirculation bubble with the ambient air, and the intermittent deflection of the supersonic annular jet corresponding to the RSS flow. The main mode f_1 stemming from the experimental data is recovered in the LES pressure signals at the center of the nozzle exit and on the lip, as well as on the DMD performed on a region of the LES encompassing the end of the divergent nozzle and a portion of the downstream jet. The second main mode f_2 is not captured at the same frequency, but two other modes are identified in preceding treatments. We also show wall shear stress distributions at the wall, thus identifying the separation and reattachment locations along the nozzle wall, and hence the boundaries of the recirculation bubble. The shear stress distributions exhibit a strong azimuthal asymmetry, which is also present in the main mode computed with a DFT.

Further work will focus on developing a better understanding the azimuthal dependence of the flow and shock patterns at the nozzle wall surface (responsible for generating nozzle side loads) on the different low-order structures located at different points in the flow. Of particular interest is the link between the central shock dynamics, the trapped recirculation bubble at the nozzle wall, and the downstream vortex ring, which can now be exploited using this spatially and temporally resolved LES model.

5 Acknowledgments

This work was carried out as part of the ATAC research group, led by CNES. Special thanks to Mr. John Valdez for performing the laboratory measurements used in this study. Support for C.E. Tinney was graciously provided through an internal research and development award with the Signal and Information Sciences Laboratory of the Applied Research Laboratories, The University of Texas at Austin.

References

- [1] A. T. Nguyen et al. "Unsteadiness of Flow Separation and End-Effects Regime in a Thrust-Optimized Contour Rocket Nozzle". In: *Flow, Turbulence and Combustion*, 71.1 (Mar. 1, 2003), pp. 161–181. DOI: 10.1023/B: APPL.0000014927.61427.ad.
- [2] J. H. Ruf, D. M McDaniels, and A. M. Brown. "Nozzle Side Load Testing and Analysis at Marshall Space Flight Center". In: 45th AIAA/ASME/SAE/ASEE Joint Propulsion Conference and Meeting AIAA Paper 2009-4856 (2009).
- [3] J. Östlund, T. Damgaard, and M. Frey. "Side-Load Phenomena in Highly Overexpanded Rocket Nozzles". In: *Journal of Propulsion and Power*, 20.4 (2004), pp. 695–704. DOI: 10.2514/1.3059.
- [4] M. Arens and E. Spiegler. "Shock-Induced Bounbary Layer Separation in Overexpanded Conical Exhaust Nozzles". In: *AIAA Journal*, 3.1 (1963), pp. 578–581.
- [5] W. J. Baars et al. "Wall Pressure Unsteadiness and Side Loads in Overexpanded Rocket Nozzles". In: *AIAA Journal*, 50.1 (2012), pp. 61–73.
- [6] G. Hagemann, M. Frey, and W. Koschel. "Appearance of Restricted Shock Separation in Rocekt Nozzles". In: *Journal of Propulsion and Power*, 18.3 (2002), pp. 577–584.
- [7] J. H. Ruf, D. M. McDaniels, and A. M. Brown. "Details of Side Load Test Data and Analysis for a Truncated Ideal Contour Nozzle and a Parabolic Contour Nozzle". In: American Inst. of Aeronautics and Astronautics. July 26, 2010.
- [8] A. Canchero et al. "Flow and Acoustics of Clustered Rockets During Startup". In: AIAA Journal, 54.5 (2016), pp. 1660–1669. doi: 10.2514/1.J054622.

- [9] E. Martelli, F. Nasuti, and M. Onofri. "Numerical Calculation of FSS/RSS Transition in Highly Overexpanded Rocket Nozzle Flows". In: *Shock Waves*, 20.2 (Apr. 1, 2010), pp. 139–146. doi: 10.1007/s00193-009-0244-4.
- [10] L. H. Nave and G. A. Coffey. "Sea level side loads in high-area-ratio rocket engines". In: 9th AIAA SAE Propulsion Conference. AIAA Paper 73-1284. Las Vegas, Nevada, 1973.
- [11] A. T. Nguyen et al. "Unsteadiness of Flow Separation and End-Effects Regime in a Thrust-Optimized Contour Rocket Nozzle". In: *Flow Turbulence and Combustion*, 71.1-4 (2003), pp. 161–181.
- [12] S. B. Verma, R. Stark, and O. Haidn. "Relationship between shock unsteadiness and the origin of sideloads inside a thrust optimized parabolic rocket nozzle". In: *Aerospace Science and Technology*, 10.6 (2006), pp. 474–483.
- [13] Y. Allamaprabhu, B. N. Raghunandan, and J A. Moríñigo. "Numerical Prediction of Nozzle Flow Separation: Issue of Turbulence Modeling". In: *Aerospace Science and Technology*, 50 (Mar. 1, 2016), pp. 31–43. doi: 10.1016/j.ast.2015.12.016.
- [14] S. Afkhami, N. Fouladi, and M. PasandidehFard. "Evaluation of Generalized K-ω Turbulence Model in Strong Separated Flow Estimation of Thrust Optimized Parabolic Nozzle". In: *Proc. Inst. Mech. Eng. Part G J. Aerosp. Eng.* 237.14 (Nov. 1, 2023), pp. 3143–3155. DOI: 10.1177/09544100231195774.
- V. Lijo et al. "Numerical Simulation of Transient Flows in a Rocket Propulsion Nozzle". In: *International Journal of Heat and Fluid Flow*, Sixth International Symposium on Turbulence and Shear Flow Phenomena 31.3 (June 1, 2010), pp. 409–417. DOI: 10.1016/j.ijheatfluidflow.2009.12.005.
- [16] S. Deck and A. T. Nguyen. "Unsteady Side Loads in a Thrust-Optimized Contour Nozzle at Hysteresis Regime". In: *AIAA Journal*, 42.9 (Sept. 2004), pp. 1878–1888. DOI: 10.2514/1.2425.
- [17] S. Deck. "Delayed Detached Eddy Simulation of the End-Effect Regime and Side-Loads in an Overexpanded Nozzle Flow". In: *Shock Waves*, 19.3 (July 1, 2009), pp. 239–249. DOI: 10.1007/s00193-009-0199-5.
- [18] A. Shams et al. "Unsteadiness in Shock-Induced Separated Flow with Subsequent Reattachment of Supersonic Annular Jet". In: *Computers & Fluids*, LES of Turbulence Aeroacoustics and Combustion 78 (Apr. 20, 2013), pp. 63–74. doi: 10.1016/j.compfluid.2012.11.016.
- [19] R. Larusson, N. Andersson, and J. Östlund. "Hybrid RANS-LES Simulation of Separated Nozzle Flow". In: 52nd AIAA/SAE/ASEE Joint Propulsion Conference. AIAA Propulsion and Energy Forum. American Institute of Aeronautics and Astronautics, July 22, 2016. DOI: 10.2514/6.2016-4670.
- [20] E. Martelli et al. "Flow Dynamics and Wall-Pressure Signatures in a High-Reynolds-number Overexpanded Nozzle with Free Shock Separation". In: *Journal of Fluid Mechanics*, 895 (July 2020), A29. DOI: 10.1017/jfm.2020.280.
- [21] B. Olson and S. Lele. "Large-Eddy Simulation of an over-Expanded Planar Nozzle". In: *41st AIAA Fluid Dynamics Conference and Exhibit*. Fluid Dynamics and Co-located Conferences. American Institute of Aeronautics and Astronautics, June 27, 2011. DOI: 10.2514/6.2011-3908.
- [22] G. Daviller et al. "Prediction of flow separation and side-loads in rocket nozzle using large-eddy simulation". In: *International Journal of Computational Fluid Dynamics* 34.7-8 (2016), pp. 622–632.
- [23] V. Jaunet et al. "Wall Pressure and External Velocity Field Relation in Overexpanded Supersonic Jets". In: *AIAA Journal*, 55.May (12 Aug. 2017), pp. 1–13.
- [24] R. Rojo, C. E. Tinney, and J. H. Ruf. "Effect of stagger on the vibroacoustic loads from clustered rockets". In: *AIAA Journal*, 54.11 (2016), pp. 3588–3597.
- [25] A. Canchero et al. "Acoustic Imaging of Clustered Rocket Nozzles Undergoing End Effects". In: *AIAA Journal*, 54.12 (Dec. 2016), pp. 3778–3786. DOI: 10.2514/1.J055053.
- [26] W. J. Baars and C. E. Tinney. "Transient Wall Pressures in an Overexpanded and Large Area Ratio Nozzle". In: *Experiments in Fluids*, 54.2 (Feb. 12, 2013), p. 1468. DOI: 10.1007/s00348-013-1468-8.
- [27] C. E. Tinney et al. "Side Load Reduction of High Area-Ratio Nozzles". In: 11th European Conference for Aerospace Sciences, Paper 598, (2025), pp. 1–15.
- [28] N. Gourdain et al. "High performance parallel computing of flows in complex geometries: I. methods". In: *Computational Science & Discovery* 2.1 (2009), p. 015003.
- [29] N. Gourdain et al. "High performance parallel computing of flows in complex geometries part 2: applications". In: *Computational Science and Discovery*, 2.November (2009), p. 015004.

- [30] T. Schønfeld and M. Rudgyard. "Steady and unsteady flow simulations using the hybrid flow solver AVBP". In: *AIAA J.* 37.11 (1999), pp. 1378–1385.
- [31] P. D. Lax and B. Wendroff. "Systems of conservation laws". In: *Commun. Pure Appl. Math* 13 (1960), pp. 217–237.
- [32] O. Colin, A. Benkenida, and C. Angelberger. "3D modeling of mixing, ignition and combustion phenomena in highly stratified gasoline engine". In: *Oil and Gas Science Tech.* 58.1 (2003), pp. 47–62.
- [33] O. Colin and M. Rudgyard. "Development of high-order Taylor-Galerkin schemes for unsteady calculation". In: *J.Comp. Phys.* 162.2 (2000), pp. 338–371.
- [34] T. Schmitt. "Large-Eddy Simulations of the Mascotte Test Cases Operating at Supercritical Pressure". In: *Flow, Turbulence and Combustion* 105 (2020), pp. 159–189.
- [35] S. Jain, R. Agrawal, and P. Moin. "Stable, entropy-consistent, and localized artificial-diffusivity method for capturing discontinuities". In: *Physical Review Fluids* 9 (Feb. 2024).
- [36] A. W. Cook and W. H. Cabot. "Hyperviscosity for Shock-Turbulence Interactions". In: *Journal of Computational Physics*, 203.2 (Mar. 1, 2005), pp. 379–385. DOI: 10.1016/j.jcp.2004.09.011.
- [37] F. Nicoud and F. Ducros. "Subgrid-scale stress modelling based on the square of the velocity gradient tensor". In: *Flow, Turbulence and Combustion* 62.3 (1999), pp. 183–200.
- [38] T. Poinsot and S. Lele. "Boundary conditions for direct simulations of compressible viscous flows". In: *J. Comp. Phys.* 101.1 (1992), pp. 104–129.
- [39] O. Cabrit and F. Nicoud. "Direct simulations for wall modeling of multicomponent reacting compressible turbulent flows". In: *Physics of Fluids*, 21.5 (2009), p. 055108. DOI: 10.1063/1.3123528.
- [40] Adrien Langenais et al. "Accurate Simulation of the Noise Generated by a Hot Supersonic Jet Including Turbulence Tripping and Nonlinear Acoustic Propagation". In: *Physics of Fluids*, 31.1 (Jan. 30, 2019), p. 016105. DOI: 10.1063/1.5050905.
- [41] Antares Development Team. Antares Documentation Release 2.3.0. 2012–2024. URL: https://cerfacs.fr/antares/.
- [42] C.W. Rowley et al. "Spectral analysis of nonlinear flows". In: J. Fluid Mech. 641 (2009), pp. 115–127.